https://doi.org/10.1016/j.nanoen.2021.106005


# Unraveling the Anomalous Mechanoluminescence Intensity Change and Pressure-induced Red-Shift for Manganese-Doped Zinc Sulfide

Li Zhang,[‡1] Kaiyuan Shi,[‡1,3] Yanlong Wang,[‡1,3] Lei Su,[*1] Guoqiang Yang,[*1] Bolong Huang,[*2] Jun Kong,[4] Xiao Dong,[4] and Zhong Lin Wang[*5,6]

[1] *Key Laboratory of Photochemistry, Institute of Chemistry, University of Chinese Academy of Sciences, Chinese Academy of Sciences, Beijing 100190, China.*
[2] *Department of Applied Biology and Chemical Technology, The Hong Kong Polytechnic University, Hung Hom, Kowloon, Hong Kong SAR, China*
[3] *Center for High Pressure Science and Technology Advanced Research, Beijing, 100094, China*
[4] *School of Physics and MOE Key Laboratory of Weak-Light Nonlinear Photonics, Nankai University, Tianjin 300071, China.*
[5] *Beijing Institute of Nanoenergy and Nanosystems, Chinese Academy of Sciences, Beijing 100083, China.*
[6] *School of Materials Science and Engineering, Georgia Institute of Technology, Atlanta, GA 30332–0245, USA.*

*E-mail: leisu2050@iccas.ac.cn (L.S.); gqyang@iccas.ac.cn (G.Y.); bhuang@polyu.edu.hk (B.H.); zhong.wang@mse.gatech.edu (Z.L.W.)

**Keywords:** Mechanoluminescence, dynamic diamond anvil cell (dDAC), high pressure, vacancies

**Abstract**
Mechanoluminescence (ML) has promising applications such as stress sensors and many other fields, which raises intensive research attention and enthusiasms in the past few decades. However, accurate characterizations of the ML process with high temporal and spectral resolution remain a considerable challenge for the current scientific community. Here, an advanced ML characterization system based on the dynamic diamond anvil cell (dDAC) is developed to achieve flexible modulations of ML performances. Upon compression, ML spectra of manganese-doped zinc sulfide (ZnS:Mn) show a large red-shift (~45 nm) and a volcano-trend of the ML intensity, and the cumulative ML intensity is solely dependent on the pressure change. DFT calculations identify the coupling of Mn-doping and surface vacancies playing a crucial role in contributing to the improvement of ML through the band offset. The suppression of the vacancies formation on the surface by the applied pressure over 4 GPa leads to the decreases of the ML intensity. This work provides a brand new ML color and intensity tuning strategy and offers a promising method to explore the ML mechanism.

## Introduction

Mechanoluminescence (ML), one of the most interesting luminescence phenomena, refers to the light emission through the mechanical stimuli, including rubbing, deforming, grinding, compressing, and cleaving, etc.[1,2] Compared with photoluminescence (PL) and electroluminescence (EL), ML is a dynamic process that is highly related to time and space. Owing to the unique feature, ML materials are promising candidates in stress sensing,[3-5] anti-counterfeiting,[6,7] and novel light source and displays.[8-11] Under the mechanical stress, the structure of ML materials undergoes various changes, including elastic deformation, plastic deformation, and subsequent crush. These enable the applications of ML for real-time and multidimensional mechanical sensing, which becomes highly significant for the safety detections in buildings and bridges[12-14]. To achieve the *in situ* monitoring of the mechanical stress change, it is strongly urgent to discover efficient ML materials and sensitive characterization techniques to reveal the change of the external mechanical stress. ML are widely identified in materials. In particular, almost 50% of inorganic salts and organic compound solids have been found to exhibit ML[15] and new ML compounds are still emerging. [16,17] Among the large amounts of ML materials, manganese-doped zinc sulfide (ZnS:Mn) is one of the most efficient ones, which shows intense ML intensity and self-recovery capability for broad applications.[18-25] Although extensive research has been carried out, the high-pressure induced ML in ZnS:Mn is still very limited. Since pressure effectively modulates the properties of photoluminescent materials (e.g., intensity, color, and lifetime [26,27]), it should not only be considered as an "excitation source" for ML. The regulation of pressure on ML materials should be explored to understand its mechanism and expand its application. Therefore, it is challenging to find an effective method to explore the in-depth underlying mechanism for pressure induced ML phenomenon.

Various methods, such as drop tower,[28,29] light-gas gun,[30,31] universal testing machine,[32,33] and atomic force microscopy (AFM),[34] have been designed to characterize ML based on the type of the stimulation. For example, the drop tower and light-gas gun methods belong to impact-based approaches, in which the light-gas gun can provide larger kinetic energy than the drop tower. Meanwhile, the universal testing machine is commonly used to drive tension or compression to polymers embedded with ML material, and the AFM method can apply stress or friction to individual ML particles. Although these techniques are pivotal in promoting the ML research, it is still challenging to accurately and precisely characterize such a dynamic process with high resolution.[35] This is due to the weak intensity and transient nature of ML. To precisely control and characterize the pressure, the Diamond Anvil Cell (DAC) equipment is often introduced[36,37], which includes X-ray diffraction (XRD), fluorescence spectroscopy, Raman scattering, ultraviolet-visible (UV-vis) absorption, and infrared (IR) to supply the information on the pressure induced change in both electronic properties and lattice structures [38]. DAC usually consists of two parallel diamond anvils with a metal gasket hole to put the sample. As the distance between the two parallel diamond anvils becomes shorter, the sample will be subjected to high pressure. To further characterize the versatile ML system with multiple compression modes (e.g., various compression waveforms, ranges, and rates), the combination with time-resolved detection (e.g., imaging and spectroscopy) is strongly desired for the further systematic investigation of the ML process.

In this work, a new ML characterization system based on dynamic diamond anvil cell (dDAC) combined with time-resolved imaging and spectroscopy is developed to specifically determine the details of the whole ML process (**Figure 1**). A systematic study of the ML process of ZnS:Mn has been carried out with this system. ZnS:Mn exhibited unique ML behavior, where an unexpected pressure-induced red-shift upon compression is noted in the ML spectra.

Meanwhile, the ML intensity increased initially and then decreased with increasing pressure. Based on the experimental verification with multiple compression modes (various compression waveforms, ranges, and times), we confirm that cumulative ML intensity solely depended on pressure change. Through the theoretical calculations, the evident optimizations of the electronic structure by the introduction of surface vacancies have been confirmed. The original interlayer structure is also strongly affected by the co-existence of applied pressure and vacancies. The opposite influences of applied pressure and the vacancy result in the volcano trend of mechanoluminescence. Our work has proposed an advanced method for flexibly tuning the color and intensity of ML through the control of high pressure, which has supplied crucial references to the understanding of ML materials and the design of efficient ML materials in the future.

**Results and Discussion**

The crystal structure, morphology, and elementary compositions of the as-synthesized ZnS:Mn particles were characterized by powder X-ray diffraction (PXRD), scanning electron microscopy (SEM), and energy dispersive spectrometry (EDS), as shown in Figure S1. The corresponding results confirmed a single-phase wurtzite structure (PDF#36–1450) with a mean size level of 1.7 μm, and the $Mn^{2+}$ dopants were uniformly distributed in the matrices.

**Figure 2a** schematically illustrates the new ML characterization system. An arbitrary function generator provides a customized waveform signal to three piezoelectric actuators to drive the dDAC and controls the synchronism between the pressure load and detection devices (details in the experimental section of Supporting Information). The pressure is measured through the ruby pressure gauge,[39] and time-resolved ML signals under dynamic pressure are collected by a fast, sensitive scientific camera and a spectrometer. Four characteristic waveforms ($\alpha$, $\beta$, ramp and sine) are designed to drive the dDAC, and the corresponding practical pressure loads are shown in Figure 2b-2e.

The ZnS:Mn particles and silicone oil (pressure transmitting medium) were sealed in dDAC at 1.1 GPa and compressed by waveform $\alpha$ to 7.3 GPa within 1 s. Waveform $\alpha$ was set to provide a constant compression rate (6.2 GPa/s). The ML process was recorded using a camera at a rate of 20 frames per second. With increasing pressure, ZnS:Mn started to emit an orange ML, which gradually became brightened and eventually turned dark red. However, the ML intensity did not always increase but decayed upon further compression and faded rapidly after 1 s (**Figure 3a**). The same result was quantitatively confirmed by spectroscopy, and the exposure time was 50 ms (Figure 3b-3d). No ML signal was detected when the pressure increased from 1.1 GPa to 1.4 GPa, and ZnS:Mn first exhibited ML with a central wavelength of 597 nm at 0.1 s (1.9 GPa). The ML emission enhanced and reached the maximum at approximately 0.35 s (3.3 GPa) when it was red-shifted to 608 nm (Figure 3b). When the pressure further increases to 3.6 GPa at 0.4s, the ML emission remains at the maximum level. Afterward, the ML was red-shifted continuously, but the peak intensity decreased under further compression, indicating the turning point at 3.6 GPa (Figure 3c). After 1 s, the pressure stayed at 7.3 GPa, and the peak positions of ML spectra remained at 642 nm, rapidly declined in intensity, and maintained its detectability until totally vanished at 1.5 s (Figure 3d). Throughout the entire compression, the ML was linearly shifted from ~597 nm to ~642 nm (Figure 3e), and such a large red-shift in ML spectral was first observed, indicating that pressure can also tune the emission color of ML. The clear linear relationship between ML peak position and pressure suggests that ZnS:Mn is a pressure-dependent functional material with potential applications in dynamic pressure sensors.

The PL properties of ZnS:Mn under pressure have been investigated before,[40,41] and the PL spectra also linearly red-shift under compression,[41] which is the same as the ML spectra (Figure S2). The main reason is that both ML and PL emissions of ZnS:Mn originate from the $^4T_1$-$^6A_1$ transition of $Mn^{2+}$ ions.[42] However, differing from ML intensity variation, the PL intensity shows a weak dependence on pressure.[41] In order to further reveal the ML process of ZnS:Mn, the variation of ML intensity was studied and the ML intensity here represents the photon number (i.e., the peak area of ML spectrum). As plotted in Figure 3f, the ML intensity under the above compression increased linearly first and then decreased gradually with a turning-point at ~3.6 GPa. The linear increase region of ML intensity has been reported before.[19, 22,43] However, the subsequent reduction has not been observed until this work.

Additionally, the ML features of ZnS:Mn upon decompression were also investigated. While unloading the pressure from 6.8 GPa to 4.0 GPa within 1 s, ZnS:Mn also showed ML, and the emission was blue-shifted continuously (Figure S3), indicating that decompression could also stimulate ML and modulate its color. Hence, the ML of ZnS:Mn is a dynamic physical process involving pressure change and absolute pressure level, which determines the intensity and color of ML. The variation of pressure can be regarded as the "excitation source" of ML under either compression or decompression. In general, large pressure changes in unit time lead to bright ML emission, but the above results indicate that the ML intensity does not always grow with pressure. The ML color of ZnS:Mn can also be regulated by pressure and the peak position related to exact pressure. To gain an insight into the ML behavior of ZnS:Mn, a term of cumulative ML intensity ($I_c$) was used to define the sum of the whole ML intensity generated before certain pressure. The plot of $I_c$ versus pressure for ZnS:Mn is presented in Figure 3g, where $I_c$ increased rapidly first and slowed down gradually over the turning-point of ML intensity mentioned above, which is well-fitted to the following theoretical equation:[24]

$$I_c = A\left(1-exp\left(-B(P-1.1)^2\right)\right), \quad (1)$$

where $A$ and $B$ represent the intrinsic constants of ZnS:Mn with values of $A=7.92\times10^7$ a. u. and $B=6.86\times10^{-2}$ $GPa^{-2}$.

The influences of compression waveform, range, and time on the ML of ZnS:Mn were systematically investigated to further verify the relationship between $I_c$ and pressure and the turning-point of ML intensity. For intuitional comparison, the normalized cumulative ML intensity was used in **Figure 4**. In addition to waveform $\alpha$, three other compression waveforms were designed ($\beta$, sine, and ramp), and their compression rates varied during compression. Through these waveforms, ZnS:Mn was compressed to ~8 GPa within 1 s (Figures S4-S6) and a consistent relationship between $I_c$ and pressure was obtained (Figure 4a). Furthermore, ZnS:Mn was compressed from 1.1 GPa by ramp waveform to different pressure levels (1.9, 2.9, 4.0, 4.9, and 6.4 GPa) within 1 s (Figure S7). In another group of experiments, ZnS:Mn was compressed to ~8 GPa under different compression times (0.1, 10, and 100 s) (Figures S8, S9, and S10). As shown in Figure 4b–4c, a good agreement was found between the $I_c$ versus pressure curves. These results indicate that the relationship between $I_c$ and pressure uniformly meets Equation (1) despite under different compression processes. It should be noted that ML spectra were collected at a fixed exposure time, but the pressure changes were different in each spectrum collection time under different compression processes. Thus, it was impossible to directly observe the change of ML intensity with pressure. Fortunately, the pressure at the maximum tangent slope of the curve between $I_c$ and pressure corresponds to the turning-point of ML intensity, so the turning-point of ML intensity under different compression processes should also at ~3.6 GPa.

We have investigated the electronic properties of ZnS:Mn under high pressure to understand the luminescence performance. Although the overall concentration of Mn doping remains the same, we have investigated the influences caused by the Mn doping near the surface to the ML performance regarding the electronic structure changes with varied thicknesses. For the thin film thickness with a higher Mn concentration near the surface, we notice the 0.30 eV band offset of Mn-3d orbitals between 1 GPa and 4 GPa and limited change after the pressure of 4 GPa (**Figure 5a**). The alleviation of the bandgap benefits the electron transfer to enhance the luminescence intensity. These results support a similar range of turning-point with the experiment. As the ZnS layer becomes thicker, such a downshifting of ZnS is still noticed. However, the scale of the downshifting is much weaker, which reduces to 0.15 eV. Similarly, the local electronic structure has remained similar after the external pressure reaches 4 GPa (Figure 5b). When the Mn concentration further decreases, it is noted that the downshifting of the Mn-3d bands is absent from 1 GPa towards 10 GPa (Figure 5c), indicating the very limited change of the local electronic structure. These results demonstrate that a higher concentration of Mn doping leads to the higher sensitivity of the local electronic structure to the external pressure, which further modifies the luminescence properties. Since anion vacancies are common defects on the surface of ZnS, we also carefully consider the effect of such defects on the electronic structure. For the higher concentration of Mn, the formation of S vacancy ($V_S$) induces an evident shrink of the bandgap of 1.34 eV, which significantly facilitates the electron transfer from the valence band under external pressure. With the increases of external pressure, the bandgap increases and becomes stable, supporting the decrease of mechanoluminescence intensity under high external pressure over 4 GPa (Figure 5d). With $V_S$ formation near the surface Mn, the alleviation to the bandgap still preserves as the Mn concentration decreases. Meanwhile, the downshifting scale of Mn-3d decreases to 0.50 eV (Figure 5e). These results confirm that the coupling between surface Mn and $V_S$ is the key to improve the luminescence performance. However, if the Mn on the surface concentration is too low, the shifting phenomenon induced by $V_S$ and Mn-doping is buried by the low sensitivity of the surface. Even with the formation of $V_S$, the PDOS has been completely pinned under different external pressure (Figure 5f). The electronic structure investigation confirms the coupling of Mn-doping and $V_S$ is the key factor to reduce the bandgap to enhance electron transfer during the external stimuli.

From the energetic perspective, the external pressure results in the stabilization of the surface structure of Mn-doped ZnS (Figure 5g), which demonstrates the higher difficulties of defect formation. To further understand the influence of external pressure, we have also studied the correlation between the doping of Mn and the formation of $V_S$. As the applied pressure becomes over 4 GPa, the energy cost of $V_S$ formation starts increasing for medium and high concentration of surface Mn doping, which remains stable or slightly decreases at further increasing applied pressure (Figure 5h). Although the formation of $V_S$ in the low concentration of surface Mn doping structure, the limited contribution to the electronic structure leads to a subtle influence on the ML performance. Therefore, these results indicate that reaching the sufficient $V_S$ concentration at high Mn doping near 4 GPa is essential to reach the optimal ML performances. Meanwhile, the formation of Mn-doping exhibits an opposite trend. As the external pressure increases, a higher concentration of Mn doping at the surface faces higher energy costs. With the external pressure, the energy cost shows an overall decreasing trend with the valley point at 4 GPa (Figure 5i). Moreover, we also reveal the structural change under external pressure. For the highest concentration of Mn-doping, the interlayer distance distribution demonstrates a peak region between 4-7 GPa (Figure 5j), indicating the largest induced polarization, which is beneficial for ML. The existence of $V_S$ leads to a tighter lattice structure when compared to Mn-doped ZnS. As the surface layer becomes thicker, the applied

pressure causes the uneven stress distribution along the surface layer, where two different trends of interlayer distance are noticed (Figure 5k). When the Mn-doping concentration becomes further lower, we notice that the interlayers of the near bulk structure show limited change while the surface structure shows high sensitivity to the applied pressure, leading to the loss of the symmetry of the ZnS lattice (Figure 5l). These results indicate that the coupling between surface Mn doping and $V_S$ significantly contributes to the increase of mechanoluminescence. Owing to the increases in the formation barrier of $V_S$ at high pressure, the optimal luminescence performance is achieved near 4 GPa with the appropriate concentration of Mn-doping.

## Conclusion

In summary, a new ML characterization system based on dDAC was developed, and multiple compression modes (various compression waveforms, ranges, and times) combined with time-resolved imaging and spectroscopy were used to study the ML process of ZnS:Mn. The pressure-induced large red-shift of ML spectra was first observed, which is ascribed to the reduction of the gap between 4T1 and 6A1 of $Mn^{2+}$ ions induced by the change of the external pressure. Most importantly, the turning-point (~ 3.6 GPa) of ML intensity upon compression and the sole dependence of cumulative ML on pressure change is revealed. DFT calculations have proved the induced band offset by the co-existence of Mn-doping and surface vacancies under pressure, which is the origin of improved luminescence performances. As the pressure increases, the formation of vacancies becomes more difficult, leading to reduced luminescence intensity under higher pressure. The in-depth reveal of the ML process of ZnS:Mn indicates that pressure is not only the "excitation source" of ML but also a significant tool to regulate the color and intensity of ML, which is of great significance to further explore the ML mechanism of more materials and expand their applications in more promising areas.

## Methods

***Material synthesis.*** ZnS:Mn particles were synthesized through solid state reaction as previously described.[27] Typically, 1.2 wt.% $MnCO_3$ (99.985%, Alfa Aesar) and 98.8 wt.% ZnS (99.99%, Acros) powders were mixed and sintered at 1100°C for 3 h under the protection of argon.

***Structural characterization.*** Sample morphology and elementary compositions were characterized by field-emission scanning electron microscopy (SEM) (SU8020, Hitachi) equipped with energy dispersive X-Ray spectroscopy (EDX) (SDD2830-300D, IXRF). Powder X-ray diffraction (PXRD) patterns of the ZnS:Mn particles were collected by the X-ray diffractometer (Empyrean, PANalytical B.V.) with Cu-$K_\alpha$ radiation.

***ML Characterization.*** Briefly, ZnS:Mn particles and a small ruby ball (pressure gauge) were loaded into a 300-μm-diameter hole in a T301 steel gasket (pre-indented to ~70 μm) on a 500 μm culet anvil. Silicone oil was used as the pressure transmitting medium. The pressure was determined using the ruby-scale method.[33] The dDAC apparatus could achieve a high-pressure load (up to 30 GPa) in a short time (less than 0.5 ms). Three piezoelectric actuators controlled by an arbitrary function generator (AFG-3051, GWINSTEK) applied load to a traditional diamond anvil cell, synchronously. By modulating the output of the arbitrary function generator (e.g., magnitude, frequency, and waveform), it was possible to study the ML behaviors of the samples under various compression ranges, rates, and waveforms. The time-resolved ML micrographs of the samples were obtained by a fast, sensitive scientific camera (pco.edge 5.5, 2560×2160 resolution, 100 frames/s) equipped on a microscope. An intensified charge-coupled device (ICCD) detector (Andor iStar, 1024×1024 resolution)

assembled with a spectrometer of 500 mm focal length (Andor Shamrock 500i, 150, 600, and 1200 gr/mm grating) allowed the collection of time-resolved ML spectra within short exposure times (>100 μs).

***Calculation Setup.*** We have applied the DFT calculations to investigate the electronic structure and energetic trend of Mn-doped ZnS through the CASTEP packages.[44] The generalized gradient approximation (GGA) and Perdew-Burke-Ernzerhof (PBE) are chosen to describe the exchange-correlation energy.[45-47] We have set the cutoff energy of the plane-wave basis set to be the ultrafine quality of 380 eV based on the ultrasoft pseudopotentials. Based on the Broyden-Fletcher-Goldfarb-Shannon (BFGS) algorithm, the k-points used in this work are applied with the coarse quality for the energy minimization.[48] For all the valence states, we treated the (3d, 4s, 4p), (3s, 3p) and (2s, 2p) for Zn, S and O, respectively. In this work, we have considered three different surface structures for the ZnS:Mn, which is constructed by 2, 3, and 4 layer-thickness. Mn has replaced the Zn atom on the surface while the S vacancy is constructed near the surface Mn. For all the models, a 20 Å vacuum space has been set in the z-axis to guarantee fully relaxation. To accomplish the geometry optimizations, the convergence test requires the total energy difference less than $5\times10^{-5}$ eV per atom and the inter-ionic displacement as 0.005 Å per atom, respectively.

**Acknowledgements**
This work is supported by the National Science Foundation of China (No. 21627802, 21771156), the Strategic Priority Research Program of Chinese Academy of Sciences (No. XDB17000000), Yong Elite Scientists Sponsorship Program by Tianjin (No. TJSQNTJ-2018-18), and the Early Career Scheme (ECS) fund (Grant No. PolyU 253026/16P) from the Research Grants Council (RGC) of Hong Kong. L. Z., K. S. and Y. W. contributed equally to this work.

**Competing interests**
The authors declare no competing financial interests.

**Reference**
[1] Walton, A. J. *Adv. Phy.* **1977,** *26*, 887.
[2] Eddingsaas, N. C.; Suslick, K. S. *Nature* **2006,** *444*, 163.
[3] Xu, C.; Watanabe, T.; Akiyama, M.; Zheng, X. *Appl. Phys. Lett.* **1999,** *74*, 2414.
[4] Sohn, K.-S.; Timilsina, S.; Singh, S. P.; Lee, J.-W.; Kim, J. S. *ACS Appl. Mater. Interfaces* **2016,** *8*, 34777.
[5] Xiong, P.; Peng, M. *J. Mater. Chem. C* **2019,** *7*, 6301.
[6] Du, Y.; Jiang, Y.; Sun, T.; Zhao, J.; Huang, B.; Peng, D.; Wang, F. *Adv. Mater.* **2019,** *31*, e1807062.
[7] Ma, Z.; Zhou, J.; Zhang, J.; Zeng, S.; Zhou, H.; Smith, A. T.; Wang, W.; Sun, L.; Wang, Z. *Mater. Horiz.* **2019,** *6*, 2003.
[8] Camara, C. G.; Escobar, J. V.; Hird, J. R.; Putterman, S. J. *Nature* **2008,** *455*, 1089.
[9] Terasaki, N.; Zhang, H.; Yamada, H.; Xu, C. N. *Chem. Commun.* **2011,** *47*, 8034.
[10] Li, W.; Huang, Q.; Mao, Z.; Li, Q.; Jiang, L.; Xie, Z.; Xu, R.; Yang, Z.; Zhao, J.; Yu, T.et al. *Angew. Chem. Int. Ed.* **2018,** *57*, 12727.
[11] Wu, X.; Zhu, X.; Chong, P.; Liu, J.; Andre, L. N.; Ong, K. S.; Brinson, K.; Mahdi, A. I.; Li, J.; Fenno, L. E.et al. *Proc. Natl. Acad. Sci. U. S. A.* **2019**, 201914387.
[12] Wei, X. Y.; Wang, X., Kuang; S. Y.; Su, L.; Li, H. Y.; Wang, Y.; Pan, C.; Wang, Z. L.; Zhu, G. *Adv. Mater.* **2016**, *28*, 6656.

[13] Wang, X.; Zhang, H.; Yu, R.; Dong, L.; Peng, D.; Zhang, A.; Zhang, Y.; Liu, H.; Pan, C.; Wang, Z. L. *Adv. Mater.* **2015**, *27*, 2324.
[14] Liu, L.; Xu, C.-N.; Yoshida, A.; Tu, D.; Ueno, N.; Kainuma, S. *Adv. Mater. Technol.* **2019**, *4*, 1800336.
[15] Jha, P.; Chandra, B. P. *Luminescence* **2014,** *29*, 977.
[16] Xie, Y.; Li, Z. *Chem* **2018,** *4*, 943.
[17] Mukherjee, S.; Thilagar, P. *Angew. Chem. Int. Ed.* **2019,** *58*, 7922.
[18] Chandra, V. K.; Chandra, B. P.; Jha, P. *Appl. Phys. Lett.* **2013,** *103*, 161113.
[19] Xu, C. N.; Watanabe, T.; Akiyama, M.; Zheng, X. G. *Appl. Phys. Lett.* **1999,** *74*, 1236.
[20] Olawale, D. O.; Dickens, T.; Sullivan, W. G.; Okoli, O. I.; Sobanjo, J. O.; Wang, B. *J. Lumin.* **2011,** *131*, 1407.
[21] Jeong, S. M.; Song, S.; Joo, K.-I.; Kim, J.; Hwang, S.-H.; Jeong, J.; Kim, H. *Energy Environ. Sci.* **2014,** *7*, 3338.
[22] Wang, X.; Zhang, H.; Yu, R.; Dong, L.; Peng, D.; Zhang, A.; Zhang, Y.; Liu, H.; Pan, C.; Wang, Z. L. *Adv. Mater.* **2015,** *27*, 2324.
[23] Zhang, Y.; Gao, G.; Chan, H. L. W.; Dai, J.; Wang, Y.; Hao, J. *Adv. Mater.* **2012,** *24*, 1729.
[24] Chandra, B. P.; Chandra, V. K.; Jha, P. *Appl. Phys. Lett.* **2014,** *104*, 031102.
[25] Chandra, B. P.; Chandra, V. K.; Jha, P. *Physica B* **2015,** *461*, 38.
[26] Li, S.; Wang, Q.; Qian, Y.; Wang, S.; Li, Y.; Yang, G. *J. Phys. Chem. A* **2007,** *111*, 11793.
[27] Ma, Z.; Liu, Z.; Lu, S.; Wang, L.; Feng, X.; Yang, D.; Wang, K.; Xiao, G.; Zhang, L.; Redfern, S. A. T.et al. *Nat. Commun.* **2018,** *9*, 4506.
[28] Xu, C.-N.; Akiyama, M.; Nonaka, K.; Watanabe, T. *IEEE Trans. Ultrason. Ferroelect. Freq. Control* **1998,** *45*, 1065.
[29] Fontenot, R. S.; Hollerman, W. A.; Aggarwal, M. D.; Bhat, K. N.; Goedeke, S. M. *Measurement* **2012,** *45*, 431.
[30] Brannon, P. J.; Morris, R. W.; Asay, J. R. *J. Appl. Phys.* **1985,** *57*, 1676.
[31] Bergeron, N. P.; Hollerman, W. A.; Goedeke, S. M.; Moore, R. J. *Int. J. Impact Eng.* **2008,** *35*, 1587.
[32] Tu, D.; Xu, C. N.; Yoshida, A.; Fujihala, M.; Hirotsu, J.; Zheng, X. G. *Adv. Mater.* **2017,** *29*, 1606914.
[33] Shohag, M. A. S.; Tran, S. A.; Ndebele, T.; Adhikari, N.; Okoli, O. I. *Mater. Des.* **2018,** *153*, 86.
[34] Sakai, K.; Koga, T.; Imai, Y.; Maehara, S.; Xu, C.-N. *Phys. Chem. Chem. Phys.* **2006,** *8*, 2819.
[35] Zhang, H.; Wei, Y.; Huang, X.; Huang, W. *J. Lumin.* **2019,** *207*, 137.
[36] Xu, J. A.; Mao, H. K., Bell, P. M. *Science* **1986**, *232*, 1404-1406.
[37] Dubrovinsky, L.; Dubrovinskaia, N.; Prakapenka, V. B.; Abakumov, A. M. *Nat. Commun.* **2012**, *3,*1163.
[38] Lee, R.; Howard, J. A. K.; Probert, M. R.; Steed, J. W. *Chem. Soc. Rev.*, **2014**, *43*, 4300-4311.
[39] Mao, H. K.; Bell, P. M.; Shaner, J. W.; Steinberg, D. J. *J. Appl. Phys.* **1978,** *49*, 3276.
[40] House, G.; Drickamer, H. *J. Chem. Phys.* **1977,** *67*, 3230.
[41] Su, F. H.; Fang, Z. L.; Ma, B. S.; Ding, K.; Li, G. H.; Chen, W. *J. Phys. Chem. B* **2003,** *107*, 6991.
[42] Bhargava, R. N.; Gallagher, D.; Hong, X.; Nurmikko, A. *Phys. Rev. Lett.* **1994,** *72*, 416.
[43] Wang, X.; Que, M.; Chen, M.; Han, X.; Li, X.; Pan, C.; Wang, Z. L. *Adv. Mater.* **2017,** *29*, 1605817.

[44] Clark, S. J.; Segall, M. D.; Pickard, C. J.; Hasnip, P. J.; Probert, M. I.; Refson, K.; Payne, M. C. *Z. Krist.-Cryst. Mater.* **2005,** *220*, 567.
[45] Hasnip, P.; Pickard, C. *Comput. Phys. Commun.* **2006,** *174*, 24.
[46] Perdew, J. P.; Burke, K.; Ernzerhof, M. *Phys. Rev. Lett.* **1996,** *77*, 3865.
[47] Perdew, J. P.; Chevary, J. A.; Vosko, S. H.; Jackson, K. A.; Pederson, M. R.; Singh, D. J.; Fiolhais, C. *Phys. Rev. B* **1992,** *46*, 6671.
[48] Head, J. D.; Zerner, M. C. *Chem. Phys. Lett.* **1985,** *122*, 264.

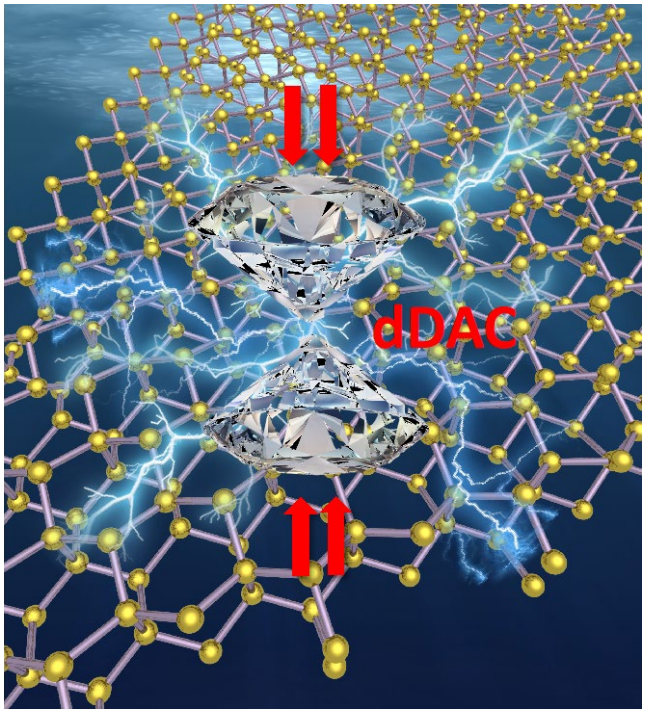


**Figure 1.** The schematic diagram for the dDAC induced mechanoluminescence in ZnS.

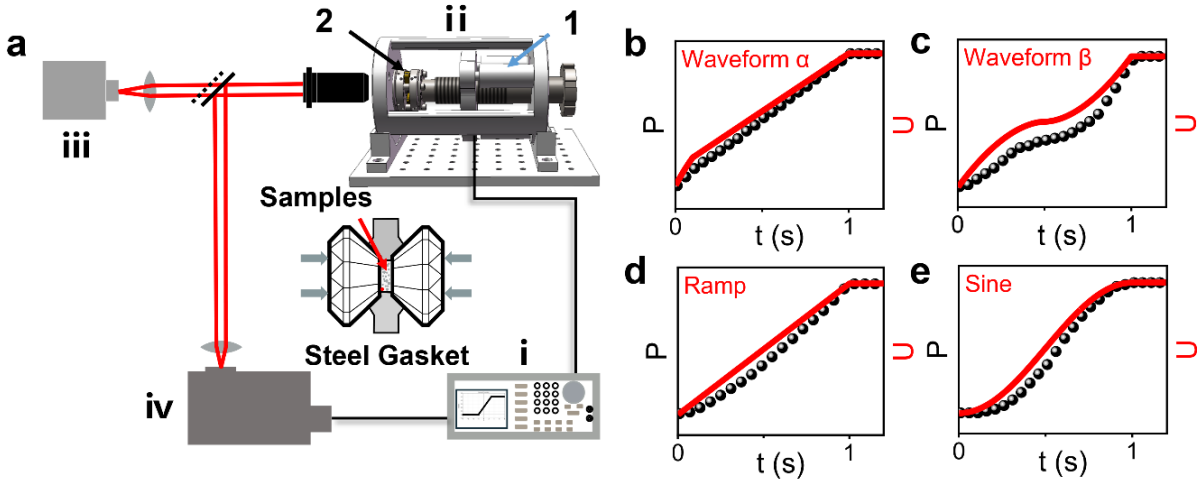


**Figure 2. Schematic illustration of the ML characterization system and four typical compression curves. a** Schematic diagram of the ML characterization system with four main components: i, arbitrary function generator, ii, dDAC (1 piezoelectric actuator, 2 conventional DAC), iii, camera, iv, spectrometer. Inset shows the schematic drawing of DAC. **b**–**e** Four waveforms (red line) output by an arbitrary function generator and black dots show the practical pressure change calibrated by the ruby pressure gauge.

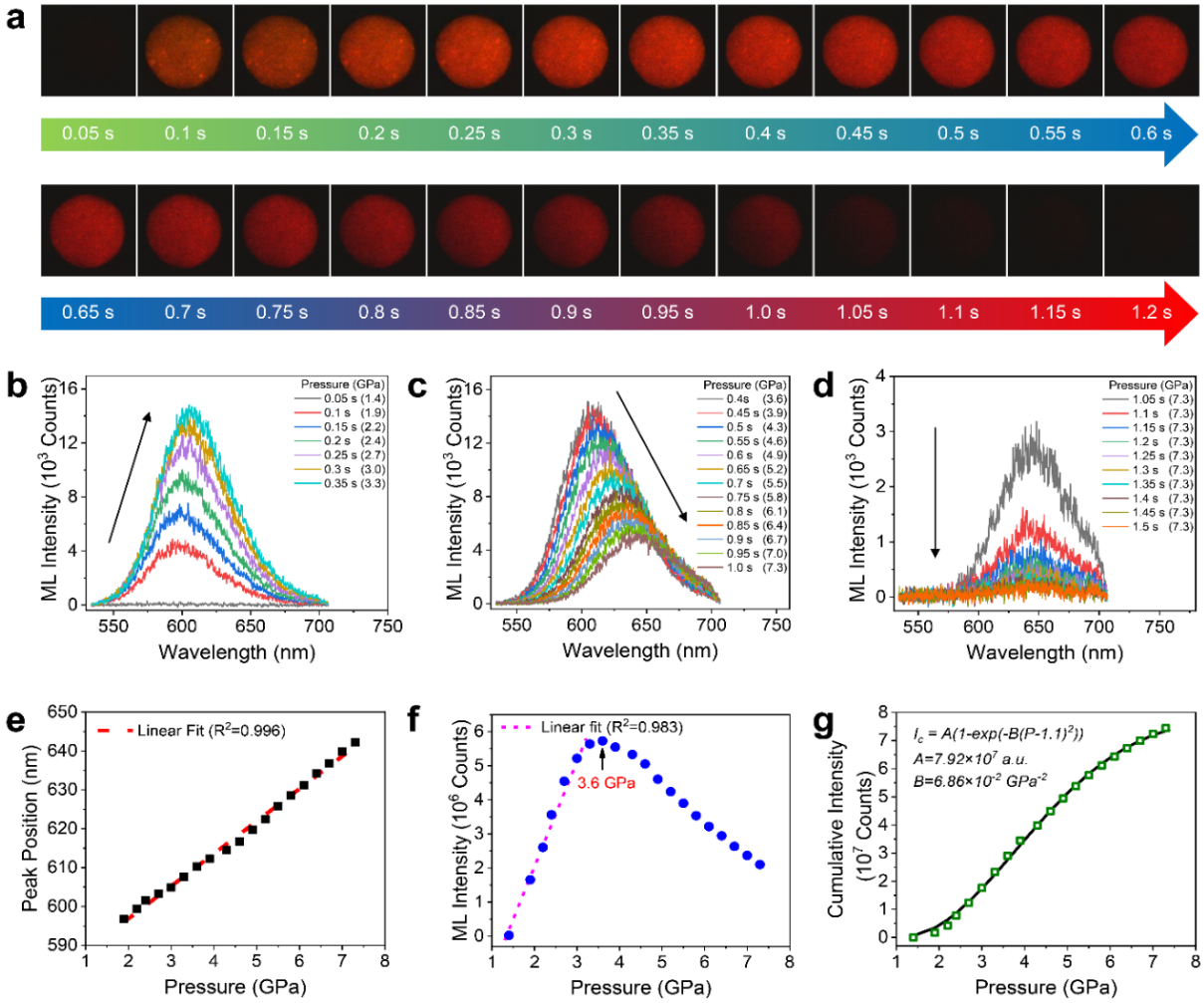


**Figure 3. ML features of ZnS:Mn compressed by waveform *α* from 1.1 GPa to 7.3 GPa within 1 s. a** Time-resolved ML photographs and **b–d** time–resolved ML spectra of ZnS:Mn with an exposure time of 50 ms. Black arrows indicate the evolution of the ML spectra as a function of time. **e** Pressure-dependent peak position of the ML spectra of ZnS:Mn. **f** Pressure-dependent ML intensity. **g** Dependence of the cumulative ML intensity on pressure.

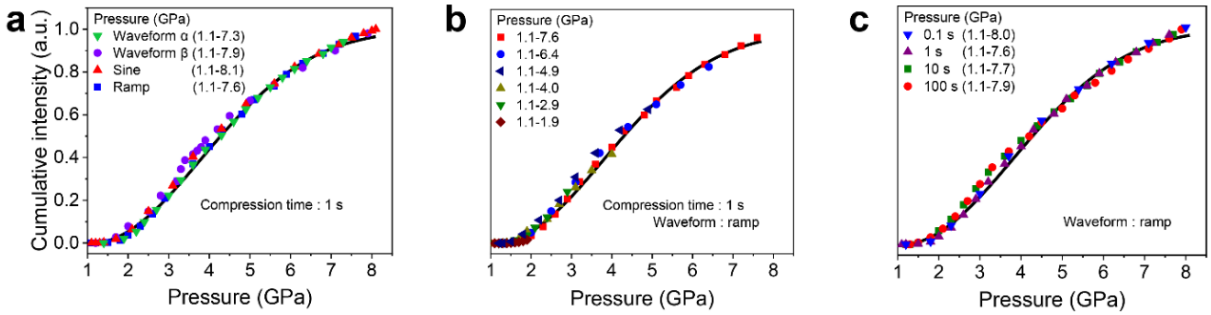


**Figure 4. Dependence of the cumulative ML intensity on the pressure of ZnS:Mn under different compression modes.** Dependence of the cumulative ML intensity on the pressure of ZnS:Mn, when (**a**) compressed from 1.1 GPa to ~8 GPa by different waveforms ($\alpha$, $\beta$, sine and ramp) within 1 s, (**b**) compressed from 1.1 GPa by ramp waveform to different values of final pressure (1.9, 2.9, 4.0, 4.9, 6.4, and 7.6 GPa) within 1 s, and (**c**) compressed by ramp waveform with different compression times (0.1, 1, 10, and 100 s) from 1.1 GPa to ~8 GPa. The black solid curve shows the fit to the normalized cumulative ML intensity on pressure corresponding to Figure 2f, and the formula is $I_c = 1.00 \times \left(1 - exp(-6.86 \times 10^{-2} \times (P - 1.1)^2)\right)$.

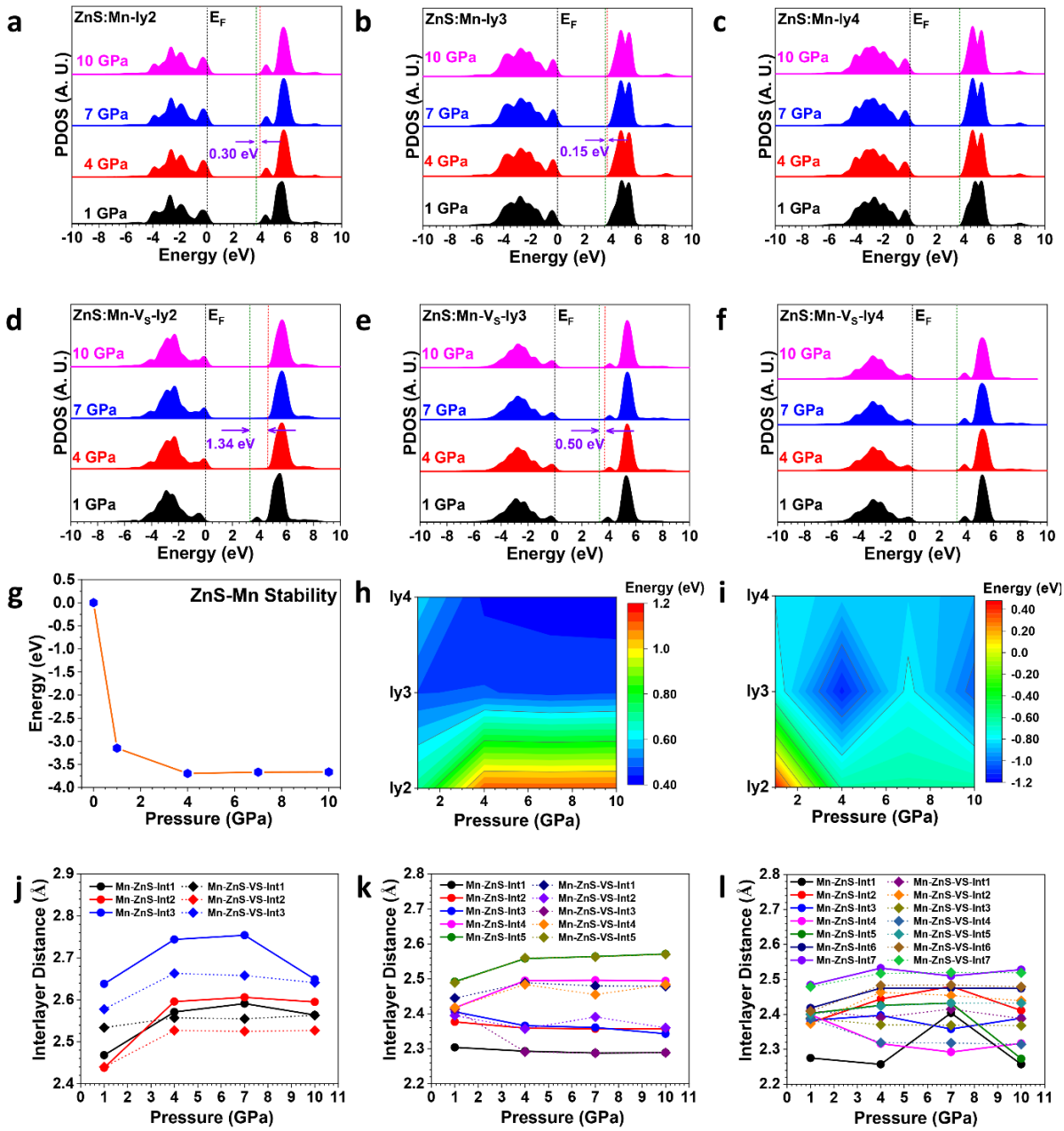


**Figure 5. DFT calculations of ZnS:Mn under external pressure. a** The PDOSs of Mn-3d of high concentration under different external pressure. **b** The PDOSs of Mn-3d of medium concentration under different external pressure. **c** The PDOSs of Mn-3d of low concentration under different external pressure. **d** The PDOSs of Mn-3d near $V_S$ of high concentration under different external pressure. **e** The PDOSs of Mn-3d near $V_S$ of medium concentration under different external pressure. **f** The PDOSs near $V_S$ of Mn-3d of low concentration under different external pressure. **g** The correlation between stability and applied pressure. **h** The energetic mapping of the formation of $V_S$ on the surface under different applied pressures. **i** The energetic mapping of Mn doping near the surface under different applied pressures. **j** The interlayer variation of high concentration Mn-doped ZnS surface. **k** The interlayer variation of medium concentration Mn-doped ZnS surface. **l** The interlayer variation of low concentration Mn-doped ZnS surface. The solid and dash lines represent the interlayers distance from the top surface to the bottom in Mn-ZnS and Mn-ZnS with $V_S$ structures, respectively.